Measurement-Driven Large-Eddy Simulations of a Diurnal Cycle during a Wake Steering Field Campaign

Eliot Quon[1]

[1]National Renewable Energy Laboratory (NREL), Golden, Colorado, USA

Correspondence: Eliot Quon (eliot.quon@nrel.gov)

Abstract. High-fidelity flow modeling with data assimilation enables accurate representation of the wind-farm operating environment under realistic, nonstationary atmospheric conditions. Capturing the temporal evolution of the turbulent atmospheric boundary layer is critical to understanding the behavior of wind turbines under operating conditions with simultaneously varying inflow and controls inputs. This paper covers the identification of a case study during a field evaluation of wake steering; the

5   development of a tailored mesoscale-to-microscale coupling strategy that captured local flow conditions within a large-eddy simulation (LES), given observations that do not completely describe the wind and temperature fields throughout the simulation domain; and the application of this coupling strategy to validate high-fidelity aeroelastic predictions of turbine performance and wake interactions with and without wake steering. The case study spans 4.5 hours after midnight local time, during which wake steering was toggled on and off five times, achieving yaw offset angles ranging from $0°$ to $17°$. To resolve these nonsta-

10   tionary nighttime conditions, the turbulence field was evolved starting from the diurnal cycle of the previous day. Given these simulated background conditions, an LES with actuator-disk turbines was compared to a steady-state engineering wake model, demonstrating agreement with measurements under partially and nearly waked conditions. The LES was also able to capture conditions during which an upstream turbine wake induced a speedup at a downstream turbine and increased power production by 10%.

1 Introduction

The atmospheric boundary layer (ABL) in which a wind farm operates is inherently nonstationary and wind turbines within

20   a wind farm must continuously adapt their behavior to harvest an evolving wind resource. More efficient and cost-effective design and operation of wind farms should therefore incorporate knowledge of not only canonical stationary conditions, but nonstationary conditions as well. Nonstationarity may arise predictably—during the morning or evening transition coinciding with sunrise and sunset, for example—or less predictably, from weather events and larger-scale atmospheric motions, or local

turbulence intermittency. The corresponding turbulent flow transients affect wind-turbine array performance through wind-turbine wake dynamics (Abkar et al., 2016) and may result in extreme wind-turbine loads (Hannesdóttir et al., 2019). High-fidelity modeling with large-eddy simulations (LES) can represent a nonstationary ABL under realistic conditions (Stoll et al., 2020; Porté-Agel, 2020), but the accuracy of that representation depends on appropriate atmospheric forcing (Bosveld et al., 2014b; Angevine et al., 2020). Having the ability to reliably simulate the ABL with a variety of site-specific, time-varying atmospheric forcings will allow wind-energy scientists and engineers to better characterize the range of wind-farm performance and wind-turbine loading that can be expected for current and future deployments.

Early LES investigations focused on quasi-steady conditions, whereas more recent studies have also included atmospheric forcings of increasing complexity and realism (Stoll et al., 2020). Here, atmospheric forcing refers to any combination of initial, boundary, or internal conditions provided to an LES to drive its solution towards known flow-field quantities, where the degree and accuracy to which the atmospheric state is known varies from study to study. Nonstationary simulations were initially performed for a diurnal cycle using approximate geostrophic wind and surface conditions derived from a near-surface sonic anemometer (Kumar et al., 2006). These earlier studies often used ad hoc parameterizations to represent the vertical structure of forcing quantities that was not known (e.g., Basu et al., 2008b; Duynkerke et al., 2004). Without comprehensive measurements including remote sensing, many researchers have turned to numerical weather prediction (NWP) for more complete representations of boundary layer profiles. A later study combined NWP with measurements, taking a similar approach to surface conditions as Kumar et al. (2006) but approximating the geostrophic wind from NWP model outputs (Kumar et al., 2010). The ability of NWP to describe the full atmospheric state, including three-dimensional velocity and temperature fields, makes them an attractive option for driving LES. As such, a large number of more recent studies have derived atmospheric forcings purely from NWP modeling at the mesoscale to more accurately simulate ABL turbulence at the microscale (Schalkwijk et al., 2015; Santoni et al., 2020; Allaerts et al., 2020; Draxl et al., 2021; Sanz Rodrigo et al., 2021)).

The spatiotemporal scales of atmospheric motion are linked in nature, but the practice of simulation across weather (mesoscale) and turbulence (microscale) regimes, also known as mesoscale-to-microscale coupling (MMC), is still gaining traction for wind-energy research and industrial applications (Sanz Rodrigo et al., 2017; Haupt et al., 2020). In addition to computational cost and model complexity (Haupt et al., 2020), numerous challenges remain in developing a robust, optimized multiscale model (Haupt et al., 2019). Modeling choices can impact the accuracy of the resulting coupled solution. There is uncertainty introduced by a wide array of NWP submodel choices, e.g., the planetary boundary layer and surface layer schemes (Yang et al., 2017; Berg et al., 2019) or the global dataset that provides mesoscale initial and boundary conditions (Kleczek et al., 2014; Rodrigo et al., 2017). Nudging techniques can improve agreement between simulated fields and observations, but introduce additional model parameters and may match trends without precisely capturing the timing of weather events (Arthur et al., 2020). Mesoscale models are further challenged by nonflat terrain, with model errors increasing at lower wind speeds and in more complex terrain (Jiménez and Dudhia, 2013). These aggregated mesoscale errors can translate into differences in hub-height wind speeds (and wind shear throughout the rotor layer) that transfer to the microscale and are reflected in, e.g., turbulent kinetic energy (TKE) and turbulent stress (Haupt et al., 2019). Microscale LES therefore only has a limited capacity to correct for the errors in the large-scale background conditions (Allaerts et al., 2020).

Despite the aforementioned challenges, MMC has been successfully applied to several wind-energy studies that included
60   modeled wind turbines operating under observed conditions. These previous investigations focused on different objectives:
turbine wake dynamics during a representative terrestrial diurnal cycle (Vollmer et al., 2017a) and offshore conditions over two
days (Vollmer et al., 2017b) for wind-farm performance during a six-day period, and turbine response to a frontal passage and
associated wind ramp (Arthur et al., 2020). Most studies used the Weather Research and Forecasting (WRF) model to simulate
the evolution of mesoscale background conditions, with the exception of one study that directly derived mesoscale tendencies
65   from an operational analysis (Vollmer et al., 2017b).

The success of these previous studies has been contingent on the availability of accurate mesoscale data from a NWP
model. This availability is not guaranteed. As an alternative to forcing the microscale with NWP model data, it is possible to
automatically derive the large-scale forcing by assimilating local observations if they are available. Allaerts et al. (2023) were
able to reproduce site-specific conditions during a diurnal cycle by using time–height profiles of wind and virtual potential
70   temperature spanning the entire depth of the computational domain, reconstructed from a meteorological tower and radar wind
profiler with an acoustic sounding system.

The objective of the work discussed herein is to apply the MMC simulation technique from Allaerts et al. (2023) to a
more challenging study. Not only is NWP not able to resolve local conditions, the available remote-sensing observations
are limited. Because the available wind and temperature data do not span the entire depth of the computational domain,
75   the partial profile assimilation approach demonstrated in Jayaraman et al. (2022) has been applied. Of particular interest is
capturing the variability of wake-steering performance under real conditions during a field campaign. This study is motivated
by the current challenges of wind-farm control, which include fundamental understanding of control flow physics and model
validation (Meyers et al., 2022) as well as the development and application of improved control algorithms (e.g., Howland
et al., 2022). The application of MMC in this context accounts for the dynamics of both the ABL and the turbine under
80   yaw-misaligned, off-design conditions.

This paper is organized into two parts. The first part details the data analysis: Section 2 summarizes the wake-steering
field campaign of interest (Fleming et al., 2019, 2020), data curation, and the case-study selection process; Section 3 then
discusses the meteorological conditions during the case study, highlighting possible simulation challenges. The second part
details the computational study. To simulate realistic evolution of the ABL before and during the study period, the MMC
85   approach is tailored for the available observations and described in Section 4. This ABL simulation is finally used to drive a
turbine simulation for the case study, presented in Section 5. The present paper focuses on turbine performance only, comparing
high-fidelity results with an engineering wake model used in wake steering controller design. An assessment of simulated wind-
turbine loads, in comparison with measurements from the field campaign, will be detailed in a companion paper by Shaler et al.
(2023) that will also include results from a mid-fidelity dynamic wake meandering model.

90   ## 2   Field Campaign

Figure 1. Site of the wake-steering field campaign, focusing on flow from the north through 5 turbines (T1–T5), with wake steering applied to T2 to benefit T3; inflow measurements come from a co-located meteorological tower and profiling lidar upstream. Maps data from Google, ©2023 CNES / Airbus, Maxar Technologies, USDA/FPAC/GEO

2.1 Overview

This study is based on measurements from the wake-steering field campaign of Fleming et al. The experimental design and demonstration of long-term wake steering effectiveness are described in Fleming et al. (2019), which details the first phase of the field campaign. The second phase of the field campaign (Fleming et al., 2020) focuses on a different set of test turbines

95 under northerly flow conditions, verifying and generalizing the results from the first phase. The present study is based on the latter campaign, which offers a longer observational period, more comprehensive data collection, and simpler inflow conditions.

The northern phase of the campaign under investigation (Figure 1) measured wake steering effectiveness in a five-turbine array that includes a central column of turbines (T2–T4), wherein the front turbine (T2) is yaw controlled, flanked by two reference unwaked turbines (T1 and T5). Wake steering through controller yaw offsets was toggled on and off at hourly inter-

100 vals, with the target offset dictated by a static optimal-offset lookup table. The instantaneous offset is a function of wind speed and direction that does not account for dynamic conditions or hysteresis effects. Only positive yaw offsets were considered, corresponding to counter-clockwise turbine yaw (viewed from above) and rightward wake deflection (viewed from upstream).

Table 1. Meteorological measurements used in this study for MMC input (I) and validation (V).

Sensor	Height [m AGL]	Measured Signal(s)	Derived Signal(s)
Pressure sensor	1.5	barometric pressure	-
Temperature/humidity sensor	2	air temperature, relative humidity	virtual potential temperature (I)
Sonic anemometer	10, 50	wind components, sonic temperature	virtual potential temperature (I), turbulence intensity (V), friction velocity (V), heat flux (I)
Temperature sensor	59	air temperature	virtual potential temperature (I)
Cup anemometer	60	wind speed (I)	-
Lidar	40–180	wind speed (I), direction (I), turbulence intensity	corrected turbulence intensity (V)

2.2 Data Sources

To characterize inflow conditions, high-frequency data from a meteorological mast were considered along with time-averaged
105 data from a co-located profiling lidar. These sensors were located approximately 160 m upwind from the leading control turbine. The met mast provided high-frequency measurements of velocity (three components), virtual temperature, humidity, and pressure. All measured quantities used for model input and/or validation are summarized in Table 1.

A number of quantities were derived from the met-mast measurements. Potential temperature calculations were based on pressure profiles, assumed to decay exponentially according to a scale height H. H was estimated from sounding data, collected
110 about 100 km away, to be 8 km. The pressure is thus evaluated as $p(t,z) = p_{obs}(t) \exp^{-z/H}$, where p_{obs} is the pressure measured at 1.5 m above ground level (AGL). Virtual potential temperatures were then calculated from the same estimated pressure profile and assuming the relative humidity (at 2 m AGL) is constant with height over the met mast. Vertical momentum and heat fluxes describing surface conditions and atmospheric stability were calculated from sonic anemometers.

The lidar data had a range gate of 20 m and a maximum range of 260 m AGL; the actual maximum range observed during
115 the case study was 180 m. Lidar-measured turbulence intensity above the 60-m-tall met mast was corrected based on lidar and cup-anemometer measurements.

In addition to the meteorological measurements, turbine operational data including power output and yaw offsets were available from NREL-installed instrumentation packages on turbines T2 and T3. Supervisory control and data acquisition (SCADA) signals were also available, providing information on all turbines. Quality assurance was performed on the SCADA
120 data using the NREL instruments. Because of the tendency for yaw signals to drift over time, the NREL experimental team regularly estimated corrections to the SCADA signal to more accurately represent the instantaneous turbine yaw position.

2.3 Case Study Selection

A study period was identified based on the availability of both quality controlled lidar wind and loads data (for the study of Shaler et al. (2023)). The availability of lidar data was considered essential for this study because the lidar captures more inflow characteristics than point measurements of wind conditions. For quality control, the lidar wind data were filtered to remove data points with carrier-to-noise ratio below -22.5 dB, while the loads data were filtered by turbine status. Only periods during which the controlled turbine (T2) and downstream turbine (T3) were operating nominally (based on turbine status codes) and producing power were considered. From the quality controlled data, candidate periods were selected with north–northwesterly winds between 320–350°, the predominant wind sector. This wind-direction range includes the direction of alignment at 324°, at which the controlled turbine (T2) directly wakes the immediate downstream turbine (T3).

Given these filtering criteria, 17 baseline (without steering) and 21 controlled (with steering) 10-min periods were found between December 2019 and January 2020, the two months of the campaign in which turbines T2 and T3 were fully equipped with loads instrumentation. The majority of the available data satisfying these criteria corresponded to atmospheric conditions with low hub-height wind speed and turbulence intensity: $U_\infty \in [5,10]$ m/s and TI $\in [1,9]$%, respectively. Out of these 38 candidates, 12 nearly consecutive 10-min periods—5 baseline, 7 controlled—occurred on 2019-12-26 after midnight, starting from 07:48 UTC (local time [LT] is UTC-7 h) and ending at 10:58 UTC.

3 Meteorological Considerations

3.1 Terrain Effects

Given northerly flow conditions, the wind flows toward the test site over mildly sloping terrain. For northwesterly flow (from 315°), the change in elevation is less than 40 m over approximately 4 km (Figure 2); the variation in elevation is less for wind directions closer to northerly (360°). Downwind of the test site, the terrain charges abruptly as the wind flows down an escarpment. A preliminary assessment of measurements near the ground (at $z = 10$ m) over a 24-hr period (2019-12-25 12:00 UTC to 2019-12-26 12:00 UTC, encompassing the 12 study periods) revealed non-zero mean vertical velocities $\sim \mathcal{O}(0.1)$ m/s, an order of magnitude larger than typical vertical motion, fluctuating with an approximately 4-hr period. Significant variability in the mean hub-height wind direction was observed over the entire duration of the case study. Whereas the wind direction ranged from approximately -135° (southwesterly) to 90° (easterly), the near-surface winds as measured by sonic anemometer varied across all directions, from -180° to 180°. No correlation was observed between the vertical velocities and the instantaneous upstream/downstream elevation changes or zonal (east–west) winds. In combination, these observations suggest the occurrence of more complex unsteady, three-dimensional flow. These wind-direction shifts near the ground may suggest atmospheric wave phenomena and be associated with turbulence intermittency (Sun et al., 2004).

Mesoscale conditions during the case study were initially simulated with the Weather Research and Forecasting (WRF) numerical weather prediction model. The innermost nested simulation domain had 3-km grid spacing. Results were insensitive to the choice of reanalysis dataset (Global Forecast System; European Centre for Medium-Range Weather Forecasts Reanalysis,
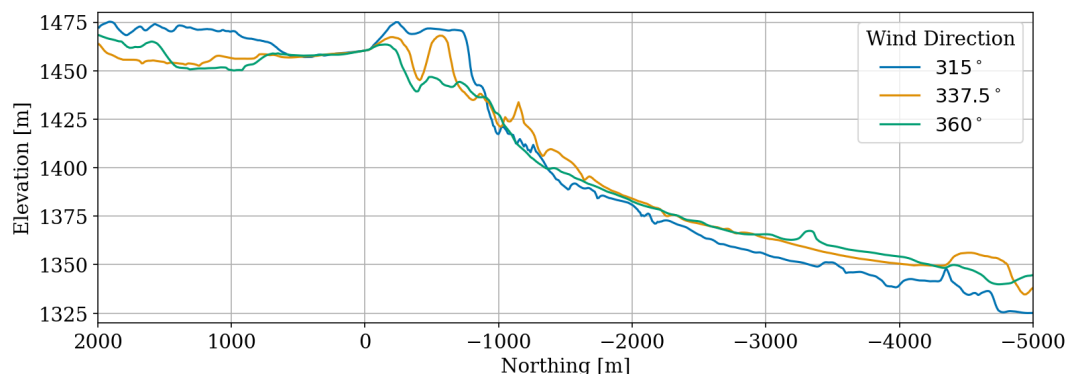
Figure 2. Terrain transects for different northerly inflow directions, centered at the field campaign location (Figure 1)

Version 5; and Modern-Era Retrospective analysis for Research and Applications, Version 2), initialization time (8, 14, and
155 20 hours before the period of interest), and planetary boundary layer scheme (Mellor-Yamada-Nakanishi-Niino Level 2.5 and
Yonsei University). Ruling out these modeling choices, the standout modeling challenge is related to terrain (see discussion
in Section 3.1). Despite the upwind terrain elevation having only mild variation, the nearest local and upwind simulated grid
locations did not agree with local observations. With terrain data resolution up to 30 arc-seconds, the flow down the escarpment
is not properly resolved by the mesoscale model. This offers additional evidence that local terrain effects such as drainage may
160 be important drivers of the mesoscale flow.

3.2 Precipitation

Analysis of synoptic weather charts indicated the presence of a stationary front that persisted throughout the period of in-
terest. Depending on the moisture in the air and the atmospheric pressure, stationary fronts may be conductive to cloudiness
and precipitation. This was confirmed by the U.S. National Oceanographic and Atmospheric Administration (NOAA) Next-
165 Generation Radar (NEXRAD), a network of S-band weather radars. Long-range base reflectivity from scans at $0.5°$ elevation
were downloaded from the NEXRAD data archive, hosted by the NOAA National Centers for Environmental Information. The
reflectivities (> 20 dBZ) indicated possible light rain in the region at 16:30 and 19:30 LT (see shaded time periods in Fig. 3).

Local met-mast observations revealed complex transport processes, the characterization of which is beyond the scope of the
present work. The onset of possible precipitation events corresponded to a sharp increase in relative humidity (RH) at 23:00
170 UTC (Fig. 3). To illustrate that this pronounced change is not due to diurnal temperature variation alone, the corresponding
evolution of RH if the absolute humidity had remained constant (from 20:00 UTC onward) is significantly lower than observed.
Observations also indicated the occurrence of temperature advection after midnight local time. Since large-scale warm air
advection from the north (given northerly flow) is unlikely, these observed changes in air temperature must be driven by
evolution of the local microclimate.
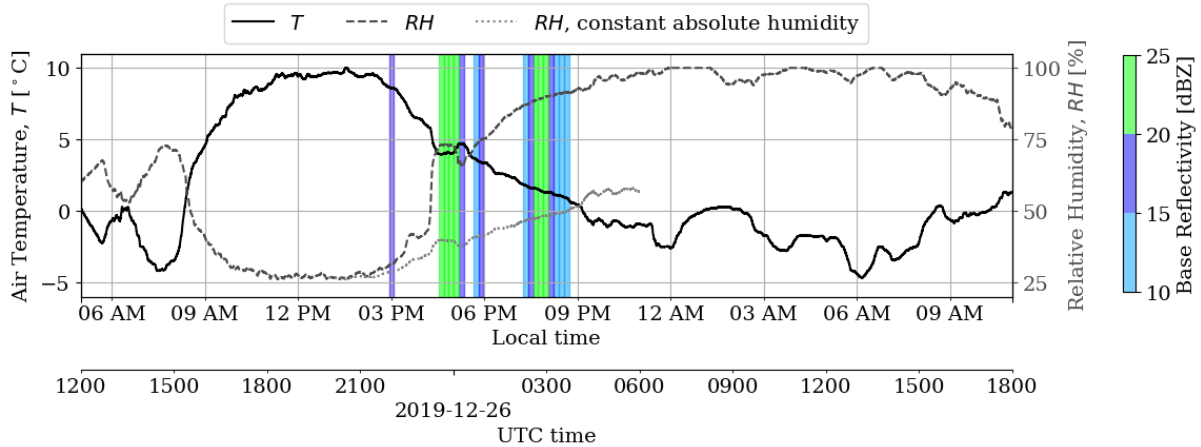
Figure 3. Air temperature (T) and relative humidity (RH) measured on the meteorological mast at 2 m AGL; shaded regions indicate 5-min periods with 10–15 dBZ (light blue), 15–20 dBZ (dark blue), and 20–26.5 dBZ (green) base reflectivity

4   A Tailored Mesoscale-to-Microscale Coupling Approach

Given the complex meteorological conditions described in the previous section, three simplifying assumptions have been made to make the computational problem approachable for wind energy modeling, the validity of which will be assessed in the present work. The first assumption is that the downstream flow down the escarpment has a negligible effect on simulated hub-height winds and, consequently, a negligible effect on wind-turbine performance, loads, and wakes. A second, related, assumption is that the upstream terrain does not induce significant inflow variation and that the observed mean vertical velocity at the met mast is negligible. In combination, these assumptions permit modeling of the entire region as having flat terrain. The third and final assumption for this case study is that the evolution of the temperature field may be decoupled from moisture transport by considering virtual temperature quantities.

Incompressible large-eddy simulation (LES) is used to resolve the locally observed atmospheric conditions and provide mean-flow and turbulence information at high spatiotemporal resolution. This LES flow-field information will complement the field measurements and provide realistic turbulent inflow conditions for coupled aeroservoelastic turbine simulations. MMC strategies are applied to realistically evolve the LES according to observed conditions. Flat-terrain assumptions permits a horizontally homogeneous ABL simulation strategy, which lends itself to profile assimilation for MMC (Allaerts et al., 2020). The specific models—Simulator fOr Wind Farm Applications (SOWFA) for LES and OpenFAST with the Reference Open-Source COntroller (ROSCO) for aeroservoelastic turbine simulation—are described in greater detail in Appendix A.

The ABL LES aims to capture the evolution of local conditions that is likely driven by larger-scale—i.e., mesoscale—nonstationarity. In general, this may be achieved by introducing source terms into the momentum and/or temperature governing equations that "nudge" the solution towards known reference values with Newtonian relaxation (Stauffer and Seaman, 1994). In contrast to observational or analysis nudging in a mesoscale four-dimensional data assimilation framework (Liu et al.,

195 2007; Telford et al., 2008) or microscale data assimilation in a detached eddy simulation (Zajaczkowski et al., 2011), which apply temporal, vertical, and/or horizontal weighting functions in three dimensions, typically near the surface, this work uses a time–height profile assimilation approach without any spatial or temporal weightings. Profile assimilation forces essential planar-averaged quantities (horizontal velocity components and/or virtual potential temperature) to match mesoscale flow information by adjusting the instantaneous momentum and/or temperature source strength Allaerts et al. (2020). These source

200 terms are horizontally uniform, taking advantage of horizontal homogeneity. Specifying time–height flow-field data based on local observations (described in Section 2.2) implicitly captures all relevant mesoscale effects including local terrain and weather. This approach was originally developed and validated with WRF mesoscale forcing and more recently demonstrated with observational forcing Allaerts et al. (2023).

The mesoscale forcing applied in the LES is derived from the instantaneous error between the simulated microscale planar

205 average and the local mesoscale flow. This forcing may either be directly applied (i.e., direct profile assimilation [DPA]) or indirectly applied (i.e., indirect profile assimilation [IPA]). In the indirect approach, the applied forcing is a polynomial representation of the direct forcing profile—this introduces interdependence between the forcing at each height level, constituting a "nonlocal" approach. Consequently, the polynomial approximation spatially filters the forcing profile and permits the microscale LES to instantaneously deviate from the enforced mesoscale trend. DPA and IPA may be thought of as a strong and

210 weak coupling strategy, respectively.

When using observations as input, initial and boundary conditions are not necessarily fully specified over the entire microscale domain. This section details the curation of the mesoscale data, reconstruction of that data to span the simulation domain over the entire simulation period, and a modified profile assimilation strategy that is compatible with the assumptions made during data reconstruction.

215 **4.1 Initial Conditions**

Considering the complexity of the observed atmospheric dynamics during and leading up to the period of interest (Section 3.2), the MMC LES was initiated during the previous morning, which saw more canonical conditions, and allowed to fully develop prior to the possible precipitation event in the afternoon. Sounding data were used to inform the initial profiles of wind and virtual potential temperature, with the closest upwind sounding site located approximately 340 km to the north. Even though

220 these are not strictly local conditions, the virtual potential temperature profiles in particular are useful for characterizing the height and strength of the capping inversion, which modulates the growth of the daytime convective boundary layer (CBL). With sounding data available every 12 hours at 00:00 and 12:00 UTC, the closest starting time was 12:00 UTC (05:00 LT) on 2019-12-25, nearly 20 hours prior to the loads study periods. This early start time should allow adequate time for the turbulence to develop in the microscale domain and adjust to any inconsistencies between the distant initial sounding and the

225 local conditions.

Sounding measurements extend from the ground up to greater than 30 km above ground level, significantly higher than the top boundary of the simulation domain. To adapt the nearest sounding to local conditions, the lowest 200 m of the wind and virtual potential temperature profiles were replaced with local site measurements (Figure 4). These profiles were linearly
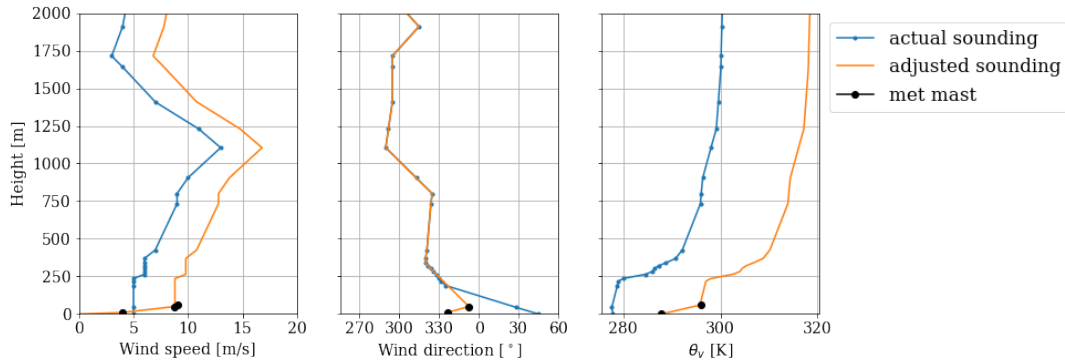
Figure 4. Upwind sounding data, adjusted with local measurements to be used as initial conditions

interpolated between measurement heights. The soundings also provided an estimate of the stable layer above the capping

230 inversion, in this case 4 K/km. This same initial value was prescribed as the fixed temperature gradient on the upper boundary.

4.2 Surface Boundary Conditions

The surface velocity is set based on Monin–Obukhov Similarity Theory (MOST) and the aerodynamic roughness height parameter, set to a nominal value of 0.1 m. In general, there is significant uncertainty associated with modeling surface conditions, in particular, when deciding how to specify the surface heat flux (see, e.g., Mirocha et al., 2015). Given measurements of tem-

235 perature and vertical velocity near the surface, the sensible heat flux may be directly calculated and specified as the boundary condition. This is appropriate for convective, neutral, and weakly stable conditions, but for moderate to strongly stable conditions, it may be more physically consistent to specify the surface temperature and derive the heat flux from MOST, thereby allowing for dynamic variation of the heat flux according to the local resolved temperature field (Basu et al., 2008a; Kumar et al., 2010). However, it should be noted that while the boundary condition sets the temperature field adjacent to the surface,

240 the entire temperature field is driven by the DPA- or IPA-derived forcing towards a known temperature profile (or value at a single height)—effectively overriding the boundary condition. This insensitivity to surface condition was confirmed by a preliminary study (not shown). Therefore, it has been assumed that when applying a profile assimilation technique that introduces source terms into the governing equations, the choice of surface boundary condition is of secondary importance. For consistency with the wind forcing and to avoid introducing excessive variation in the temperature forcing, the history of surface

245 heat flux (rather than surface temperature) has been specified to keep the surface conditions quasi-stationary within the 10-min forcing timescale (corresponding to the temporal resolution of the available wind profile data).

Daytime convective conditions were simulated by specifying the kinematic heat flux calculated from sonic anemometer data at 10- m AGL. The preliminary study found that an assumption of a constant flux surface layer was invalid — specifying the 10-m heat flux at the surface resulted in only 80% of the observed flux at 10 m, which had a maximum of 0.1 K-m/s (indicative of

250 weakly convective conditions). Therefore, the specified surface heat flux was increased by 25% to match observed conditions.
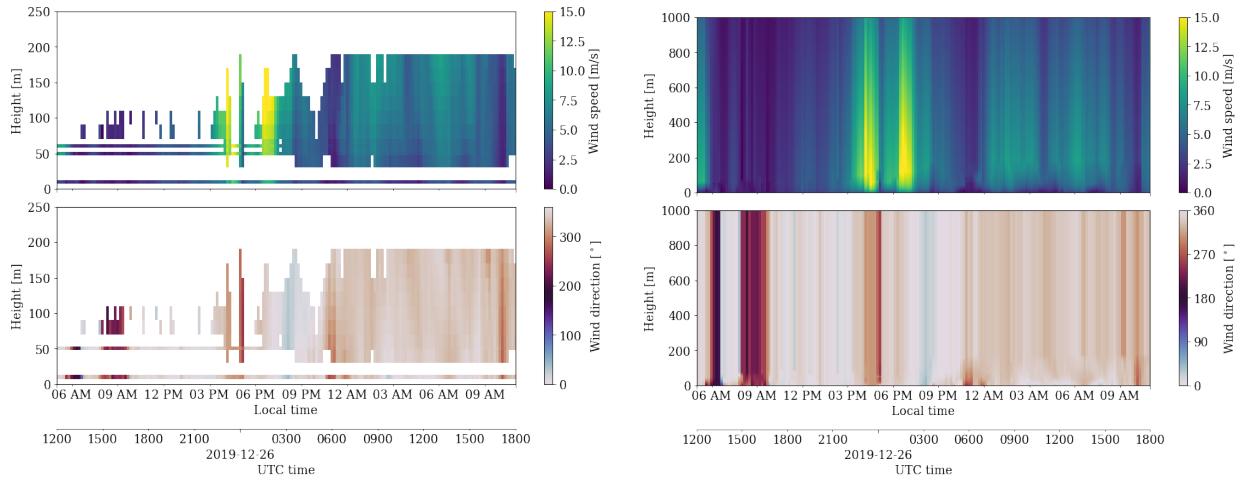
Figure 5. Available wind speed and direction measurements including sonic anemometers, cup anemometer, and lidar, shown up to the farthest lidar range gate (left panel); reconstructed time-height wind profiles, spanning the vertical extent of the computational domain (right panel)

In the nighttime, the empirical rescaling was not applied. To more accurately represent the observed nocturnal temperature advection (Figure 3, after midnight LT), the observed temperature on the met mast at 59 m was also assimilated.

4.3 Partial Profile Assimilation

A wind time–height history was reconstructed for MMC (Figure 5) following a procedure specific to the data available for this study. The procedure included quality control, fitting instantaneous profiles to a canonical power law, and interpolation, and is fully detailed in Appendix C. The final reconstructed wind-speed profiles had wind shear with power-law exponent (α) of approximately 0.1 in the daytime between 09:00–14:30 LT; then, the shear increased, varying between $\alpha = 0.2$–0.4 throughout the remainder of the afternoon and into the evening. Between 22:00 LT and midnight, the shear was highly variable not well defined by the power law when taking into account all available wind measurements. From 01:00 LT and onward the next day (during the turbine study period) α similarly varied between 0.2–0.5.

The flow-field reconstruction provides a representation of how the background wind profiles evolved, but the available measurements did not support any reasonable approximation of how the temperature profile evolved. Information about the thermal stratification and ABL height would have informed the reconstruction of the wind profiles above the ABL; moreover, temperature profile assimilation could have been performed alongside the wind profile assimilation. Instead, the evolution of the temperature profiles in the current study is more idealized, dictated only by initial and surface conditions.

An additional consideration is needed because the height of the ABL is not known. The reconstructed winds (Figure 5) are only valid within the ABL and at the top of the ABL the boundary layer winds should transition to geostrophic and thermal winds. However, it is not known whether a geostrophic or thermal-wind balance exists, or how the free atmosphere interacts

with the ABL. An additional assumption must be made, falling back on a simpler assimilation strategy. Instead having the large-scale forcing vary in both time and height, the forcing is assumed to be uniform with height and vary in time only. Then, to capture both local mesoscale variability near the ground and allow realistic ABL evolution aloft, the wind forcing profile is blended from the forcing profile derived from profile assimilation to a constant value. Ideally, transition between the height-varying ABL forcing and the uniform free-atmospheric forcing would occur at the instantaneous ABL height, but because this height is not known a priori, the transition between the forcing regions occurs above 180 m, the highest available measurement. Above 180 m, the vertical gradient of the forcing profile is linearly scaled to zero. The thickness of the transition layer was chosen to be 100 m. This approach has been recently applied in a similar fashion with virtual potential temperature profiles (Jayaraman et al., 2022, "Hybrid II" strategy).

5   Results & Discussion

The LES setup is detailed in Appendix B. Section 5.1 first presents the measurement-driven precursor simulation of the diurnal cycle leading up to and during the case study period. Then, Section 5.2 presents LES results with turbines represented as actuator disks, driven by the nonstationary conditions of the precursor. Section 5.3 derives additional insights from these results.

5.1   Diurnal Cycle Simulation with MMC

An initial investigation compared four different assimilation approaches to applying mesoscale forcing throughout the selected case day. The simplest approach is to apply a time-varying uniform forcing, which can only force the simulated wind profile to match the mesoscale data at a single reference height level. In this case, the reference height was chosen to be 50 m—the height of the highest sonic anemometer, which provided the most reliable, highest resolution wind measurement. For comparison, the direct and indirect profile assimilation approaches of Allaerts et al. (2020) (DPA and IPA, respectively) were also applied. Lastly, the partial profile assimilation approach detailed in Section 4.3 was also considered. Separate assimilation approaches were considered for daytime and nighttime, with the switchover occurring at 14:00 LT just before the measured change in atmospheric conditions (Figure 3).

Given the apparent temperature advection during both the diurnal and nocturnal periods (Figure 3), the only available temperature measurement (temperature probe at 59 m height) was assimilated, corresponding to uniform forcing based on a single level. To highlight the impact of the single-level temperature assimilation, the simplest single-level wind forcing (at 50-m AGL) case is considered with and without temperature forcing during the daytime. Even when temperature and humidity are not changing significantly due to weather, assimilating local temperature observations can change the structure of the capping inversion, which in turn alters the geostrophic wind and, consequently, also affects the veer throughout the ABL (Figure 6). All other simulations used single-level temperature assimilation.

The paucity of daytime measurements adds uncertainty to the flow-field reconstruction (Figure 5) and results in varied wind profiles (Figure 6). DPA appears to predict an extremely shallow convective ABL while IPA appears to predict a sharp low-level
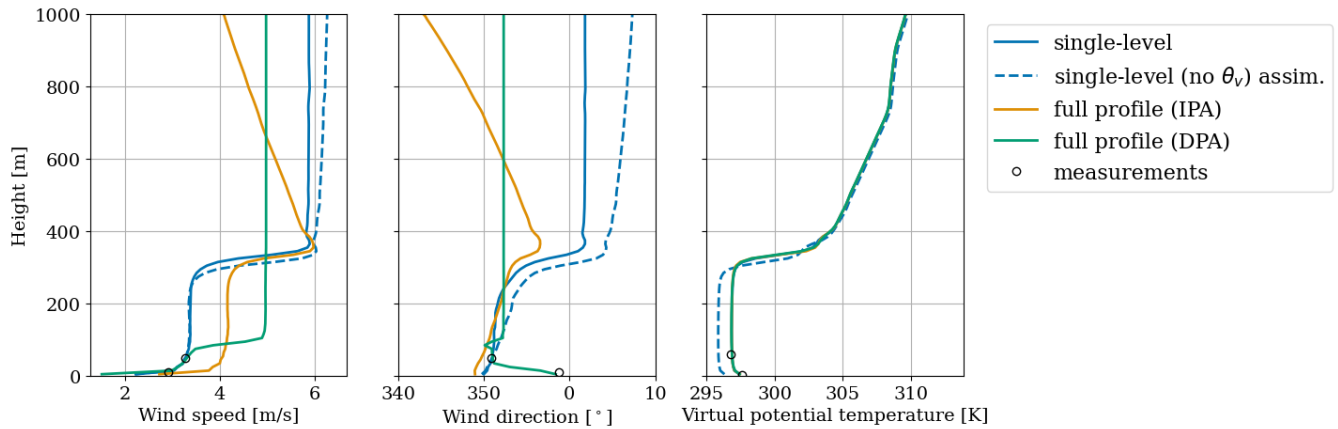
Figure 6. Example daytime CBL profiles at 13:00 local time for various mesoscale forcing approaches; markers indicate the available sonic anemometer measurements
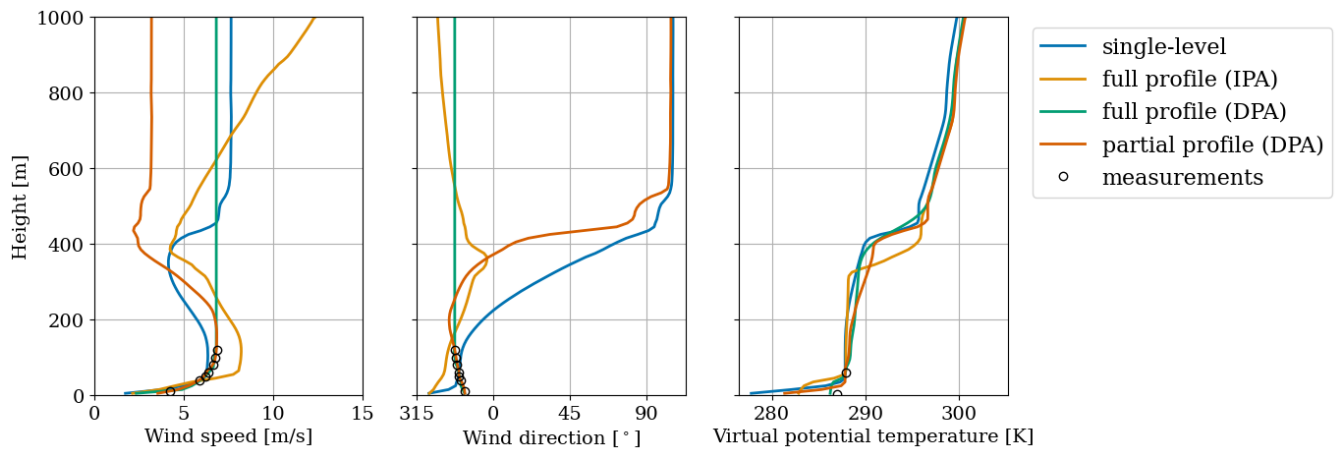
Figure 7. Example nighttime stable boundary layer profiles at 01:00 local time for various mesoscale forcing approaches; markers indicate the available sonic anemometer and quality controlled lidar measurements

jet in the daytime—neither of which appear plausible. The possibility of unbounded IPA behavior is a known issue (Allaerts et al., 2023). In contrast, the single-level results (assimilating winds at 50 m) predict the most reasonable representation of the weakly convective boundary layer and overlying free atmosphere, while also capturing the observed wind speed at 10 m.

In the nighttime, a larger range of wind speed and direction values are observed than in the daytime; the thermal structure of the boundary layer also shows more variation due to the cumulative differences in both wind and temperature profiles over the course of the day (Figure 7). Single-level assimilation is unable to represent the observed wind profile, instead predicting a very shallow low-level jet. The IPA results are once more suspect, with high wind speed and shear simulated at the top of the computational domain. Therefore, plausible results include the full- and partial-DPA simulations, with pronounced differences

in the free atmosphere. Under these conditions, the partial-DPA LES predicts lower wind speeds aloft that describe a nocturnal
310   low-level jet.

Quantities of interest were calculated for all four approaches (Figure 8). The time-history of the simulated case day clearly demonstrates that the mean wind speed and direction trends from experiment are generally reproduced. Because the IPA approach allows the microscale to deviate from the input mesoscale data — a potentially desirable mechanism for modulating mechanical turbulence production (Allaerts et al., 2020) — some differences $\sim \mathcal{O}(1)$ m/s are seen. Turbulence intensity (TI),
315   turbulence kinetic energy (TKE), and friction velocity are not directly specified but also capture the observed trend in all cases. Excluding outliers, the TI in the daytime is several times higher than in the nighttime: 20–30% compared to 5–10%. TKE provides a similar assessment that also takes into account vertical velocity variance and does not have sensitivity to low wind speeds. At night, the turbulence is intermittent. Some of this variability is captured with the various assimilation approaches but the timing and magnitude do not exactly match observations (from 22:00 LT to the end of the simulation) in terms of
320   turbulence intensity and friction velocity.

5.2   Turbine Simulation during Study Period

Results from the SOWFA–OpenFAST aeroelastic turbine simulation and the engineering-fidelity FLOw Redirection In Steady state (FLORIS) wake model are compared with the power signal recorded by the wind-farm Supervisory Control and Data Acquisition (SCADA) system. The ABL LES for the turbine study was restarted from the daytime CBL simulation with single-
325   level forcing wind and temperature forcing; from this fully developed turbulence field the evening transition and nocturnal stable boundary layer were simulated with partial-wind-profile DPA and single-level temperature assimilation. Mean wind conditions, which were also the inputs to FLORIS, showed reasonable agreement with lidar observations (Figure 9). During the selected turbine analysis periods, the simulated wind speed ranged between 4–7 m/s, the wind direction was approximately north–northwesterly, and the TI ranged between 2–10%. While the TI is in a similar range as the observations, the timing of
330   the turbulence intermittency is not reproduced.

Wake steering is toggled on and off by manipulating the input yaw signal to the turbine controller, resulting in an intentional yaw misalignment. Periods without any commanded yaw offset will also see unintentional yaw misalignment due to turbulent fluctuations of the wind vector magnitude and direction. Similarly, the actual yaw offset achieved will differ from the commanded optimal offset due to turbulent fluctuations (Figure 10c). Note that SCADA data are available throughout the study
335   period, but only the 10-min periods during which all NREL-collected data channels passed QA/QC have been highlighted.

All reported power output (Figure 10) has been normalized by the mean of freestream reference turbines T1 and T5. Between 07:48 UTC and 08:18 UTC, the true measured yaw offset is approximately 0°. However, the wind direction is offset from the T2–T3 alignment direction (324°) by 8° resulting in partial waking of T3 by T2 (Figure 11a). During this time, the simulated and measured wind speed and direction differ by up to 0.2 m/s and 2.1°, respectively, but the TI is underpredicted in the LES
340   (2%) whereas in reality the TI jumped from 4–9%. Both SOWFA and FLORIS are in agreement with the measured power from T3 (Figure 10).
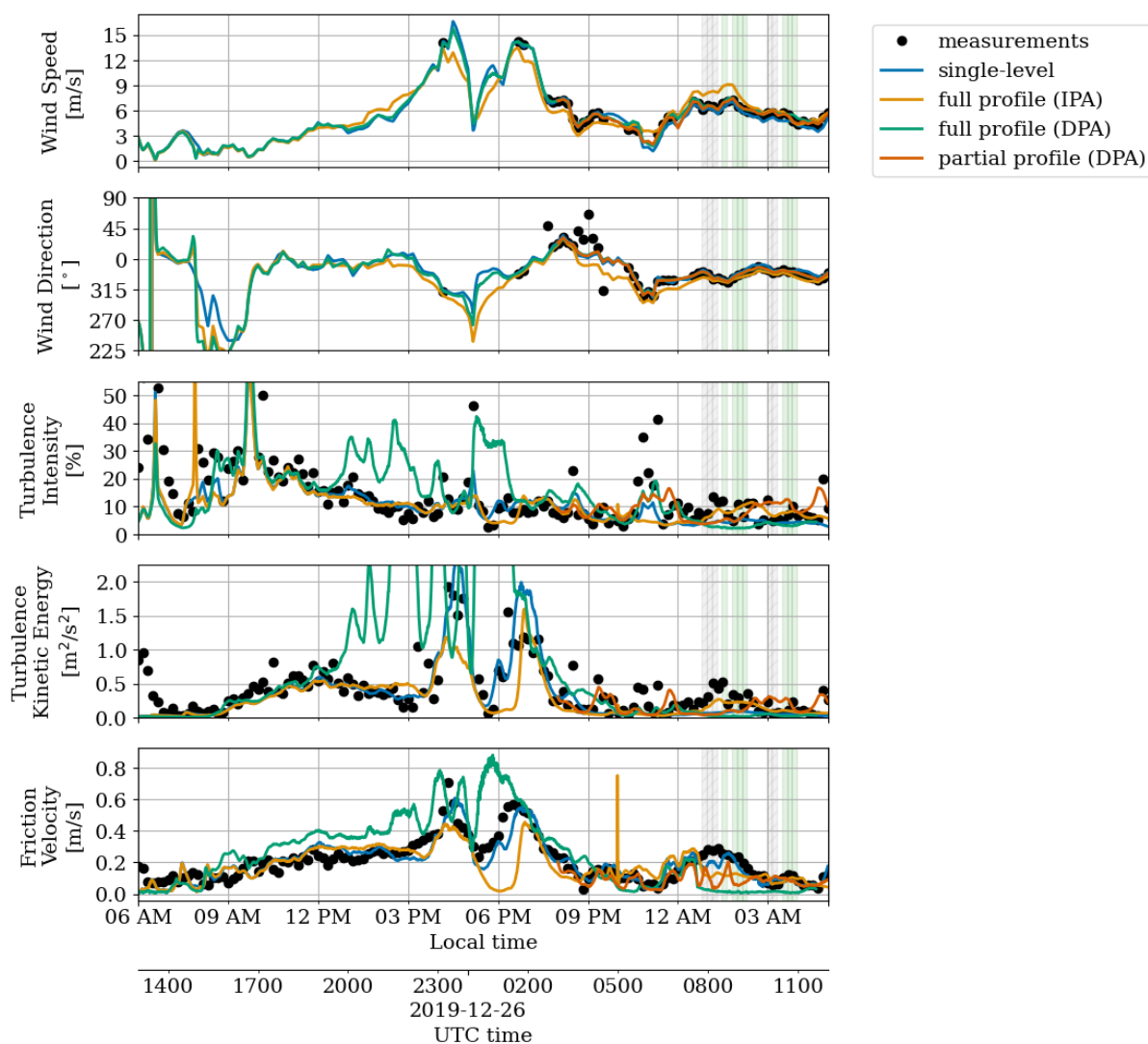
Figure 8. Simulated atmospheric conditions during the full coupled LES (lines) in comparison with measurements (symbols): hub-height lidar wind speed and direction, 50-m sonic-anemometer turbulence intensity, 50-m sonic-anemometer turbulence kinetic energy, and 10-m sonic-anemometer friction velocity; 10-min periods of interest for turbine analysis are highlighted (no yaw offset commanded: gray shading with hatch marks; commanded yaw offset: green shading)
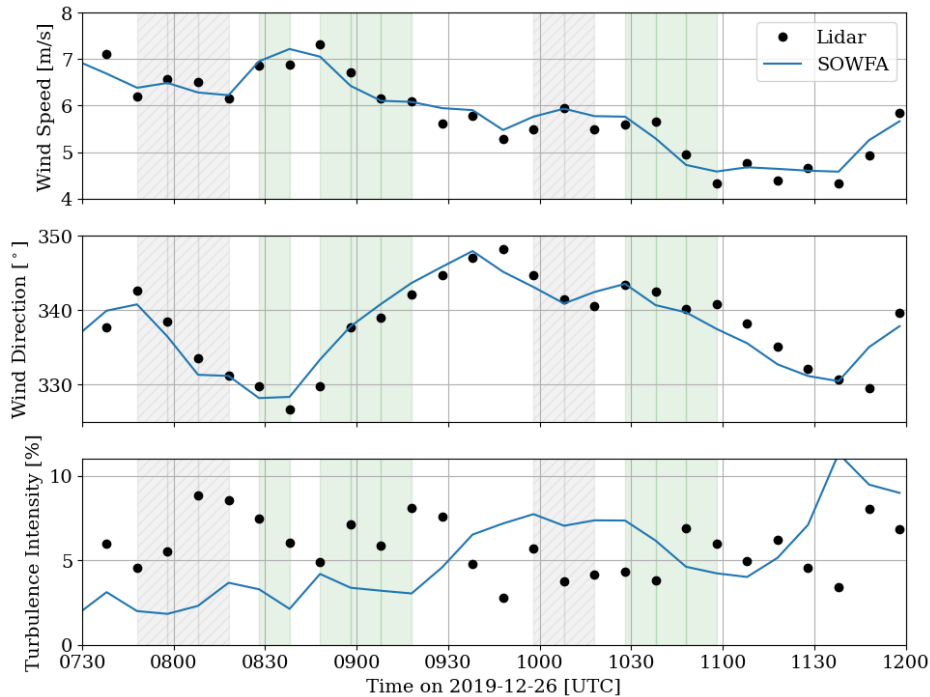
Figure 9. Ten-minute mean wind speed, mean wind direction, and turbulence intensity at hub height throughout the turbine study during periods without any commanded yaw offset (gray shading with hatch marks) and a commanded wake-steering offset (green shading)

The subsequent wake-steering period from 08:28 UTC (Figure 10) had a simulated wind-speed and direction in agreement with measurements to within 0.2 m/s and 1.7°, while achieving the largest yaw offset of the whole study, 17°. The TI was still smaller by a factor of 2. This was less than the commanded offset of 25° and resulted in a similar partial waking scenario as the previous period without steering (Figure 11b). At this time, SOWFA correctly predicts the waked conditions whereas FLORIS appears to represent unwaked conditions. However, in the remainder of this steered period from 08:48 to 09:28 UTC, both SOWFA and FLORIS predict completely unwaked conditions. After 09:08 UTC, the wind direction appears to be sufficiently offset from the T2–T3 alignment direction such that, despite a reduction in wake steering offset, the downstream turbine produces power as if it were in the freestream.

During the next highlighted periods without steering from 09:58 UTC (Figure 10), there appears to be further interplay between the wind direction and turbine yaw. During this time, the simulated wind-speed and direction agree with measurements to within 0.5 m/s and 1.6°. Even though the actual yaw is nonzero, there is enough wind-direction offset such that the T3 power output is close to freestream output through 10:48 UTC (Figure 11c). In fact, there are several 10-min periods observed in the field (3 periods) and in the LES (2 periods) during which the downstream turbine power production exceeds freestream power by approximately 10%.During the nearly-waked conditions between 10:18 and 10:28 UTC for instance, the excess power
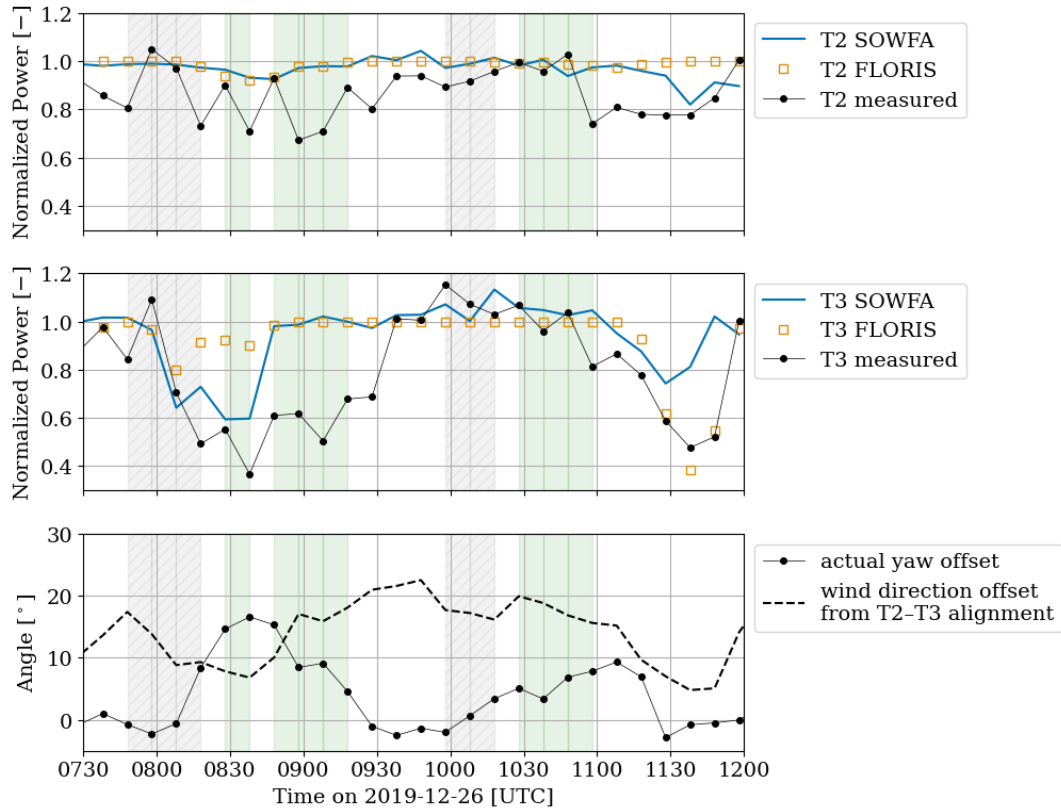
Figure 10. Normalized 10-min mean power for turbines T2 and T3 (panels (a) and (b), respectively) during periods without any commanded yaw offset (gray shading with hatch marks) and a commanded wake-steering offset (green shading); the actual measured offset is given in panel (c), along with the degree to which T3 is directly waked by T2

produced by T3 is associated with a 2–4% increase in wind speed seen by the turbine. This estimated wind-speed increase is a spatial average over the rotor disk, and varies depending on upstream location.

From approximately 11:38 UTC onward (Figure 9), there appears to be a change in simulated mesoscale conditions seen in the wind direction and TI. The condition change appears to arise 10 to 20 min early, for wind direction and TI, respectively,
360   compared to observations. This corresponds to the mismatch between measurement and LES for both T2 and T3 (Figure 10).

5.3   Discussion

Nocturnal stable boundary layers, even without turbulence intermittency, are challenging to simulate (Bosveld et al., 2014a). Despite the mismatch in TI histories (Figure 9), Figure 10 shows good agreement between the LES and measured performance of T2 and T3, under both partially-waked (between 08:00 and 08:30 UTC) and nearly-waked conditions (i.e., when T2's wake
365   is close to impinging on T3, between approximately 10:15 and 10:45 UTC). Even though the simulated and measured TI may have differed by up to a factor of 4, the quality of these comparisons suggests that the turbulence regime (TI < 10%) rather than
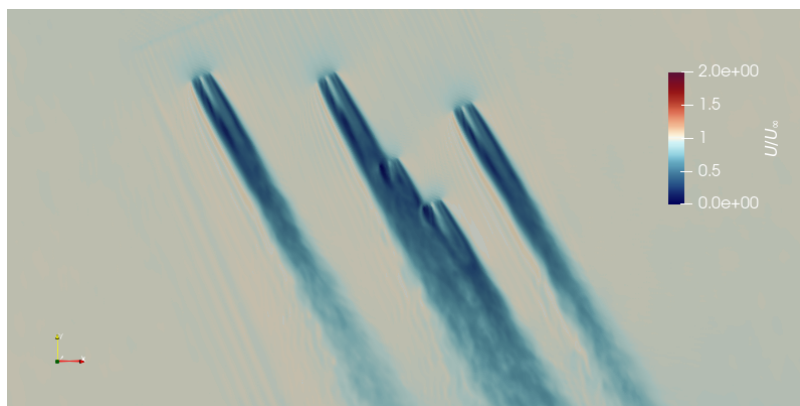
(a) $S = 6.5$ m/s, $D = 332°$, $TI = 2\%$ with $\psi = 0°$ (08:08 UTC)
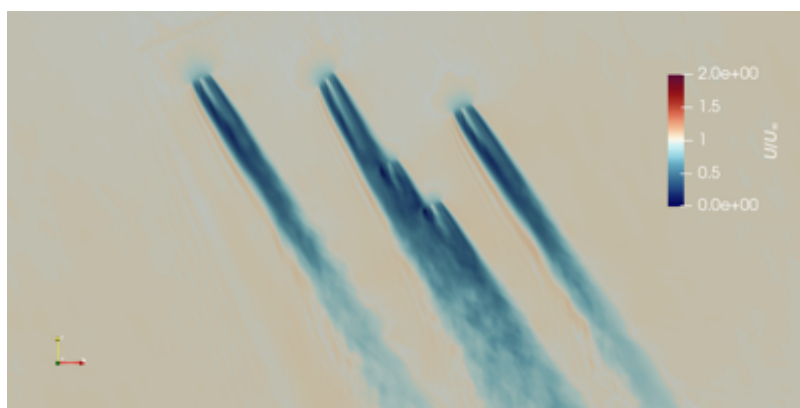
(b) $S = 7$ m/s, $D = 328°$, $TI = 3\%$ with $\psi = 15°$ (08:28 UTC)
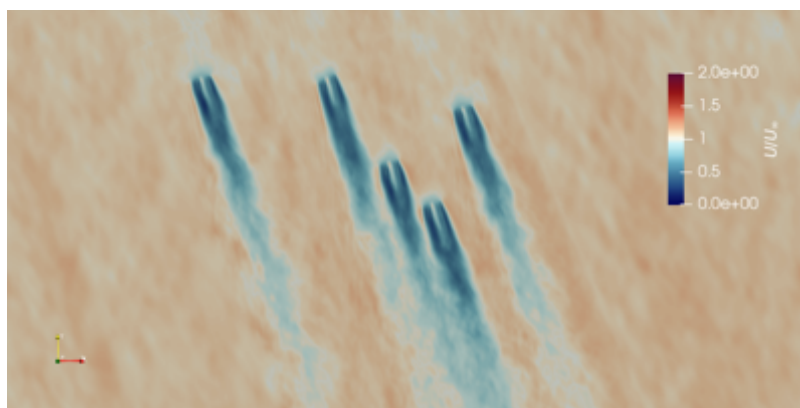
(c) $S = 6$ m/s, $D = 343°$, $TI = 7\%$ with $\psi = 4°$ (10:18 UTC)

Figure 11. Ten-minute mean horizontal wind-speed fields at wind-turbine hub height predicted by LES on 26 Dec 2019, normalized by the inflow wind speed; the mean wind speed (S), wind direction (D), turbulence intensity (TI), and actual yaw offset (ψ) are given.

the instantaneous magnitude of TI is the more important driver of turbine–turbine wake interactions. However, it is important to note that this difference in background turbulence may have a more pronounced impact on turbine loads than performance.

370   The simulated and measured power can have discrepancies when the wind-direction offset (from the direction of alignment between T2 and T3) combined with the instantaneous yaw offset result in borderline waked conditions (i.e., partially or nearly waked). These borderline conditions may arise from small differences in the simulated and actual wind direction, e.g., between 08:48 and 09:28 UTC. Uncertainties in the wind-field reconstruction may have affected the quality of both the LES and engineering model predictions.

375   In addition to the sensitivity to instantaneous wind direction, the actuator disks in the LES generate some numerical artifacts (the "streamers" seen emanating from the edges of the rotors in Figure 11b). These types of artifacts, which may be obscured by the background flow under conditions with higher turbulence intensity, are due to application of a second-order central-difference numerical scheme with insufficient grid resolution to capture the velocity gradients around the rotor. To eliminate these numerical oscillations, the grid resolution would need to be increased by a factor of 10^6 to strictly satisfy a grid resolution constraint for grid Péclet number Pe ≤ 2 (Xu and Yang, 2021), making a 4.5 hr turbine LES far from tractable. However,

380 spurious waves do not necessarily impact rotor performance and loads if $\mathcal{O}(10)$ grid points are simulated across the rotor (Revaz and Porté-Agel, 2021), a condition which is satisfied by the present LES setup.

    The engineering and LES models are generally in agreement, with FLORIS clearly indicating when partial or full waking is expected to occur (Figure 10). Differences were seen under three conditions: when FLORIS overpredicts the effect of steering, when there is a wake-induced speedup, and when there are dynamic inflow conditions. When steering is overpredicted, there

385 is less waking and higher downstream turbine performance than observed in the LES and field measurements. This may be remedied in FLORIS by using the inflow TI as a tuning parameter (Doekemeijer et al., 2022). Because FLORIS does not simulate the flow field, effects such as blockage and the resulting speedup cannot be modeled unless a representative heterogeneous inflow field is provided as input (e.g., Branlard and Meyer Forsting, 2020). Similarly, FLORIS does not model wake motion, which would require a dynamic wake model. This actually translated into a more accurate prediction of T3

390 power production during the case study at around 11:38 UTC—because the simulated wind-direction shift was earlier than observed (Figure 9), the specified T2 position history (for 0° offset during this period) in the LES would have lagged behind the simulated wind direction change. This temporal shift in the LES resulted in an earlier reduction in waking on T3 and a large discrepancy between LES and measurement. Under steady conditions, however, the engineering model continued to track the performance of T3 measured in the field.

395   While the simulated wind-field statistics (Figure 9) are not in exact agreement with lidar observations, most notably in terms of the time history of the hub-height turbulence intensity, the resulting ABL simulation for the full day appears to be a reasonable representation of evolving mesoscale conditions—especially given the predicted turbine performance trends over a 4.5-h period (Figure 10). As seen in Figure 6 and Figure 7, different plausible (and implausible) realizations of the ABL are possible. Differences in flow-field realizations may be attributed to a combination of surface condition modeling, terrain,

400 neglected large-scale vertical motions, and initial conditions. These uncertainties have varying degrees of importance depending on the time of day. During the daytime, any local terrain-induced wind variability is likely to be eliminated by turbulent mixing

in the CBL, while in the nighttime this variability might be more pronounced. The ABL realization produced by partial-profile DPA, ultimately used for the turbine study, results in a low-level jet with nose near the top of the rotor (Figure 7); the ad hoc transition thickness (100 m) used in the partial profile assimilation does not appear to produce any appreciable wind profile
405 anomaly between 180 m and 280 m AGL. The formation and evolution of this jet, however, may create shear instability and be responsible for the observed intermittent turbulence (Figure 9c). The current partial profile assimilation approach is not intended to be a one-size-fits-all strategy. More sophisticated strategies are possible, for example, estimating the instantaneous boundary layer height from the resolved turbulence fluxes. Overall, the extent to which field conditions are reproducible with MMC depends on the nature of the background physical phenomena and their observability.

6 Conclusions

This work has provided insights into the practical applicability of MMC techniques given limited atmospheric data at a specific site. In this case, the limitations include the lack of information about the wind profile above 180 m in the nighttime and above 50 m in the daytime; lack of information about the temperature profile apart from point measurements at 2-m and 59-m AGL; and the inability of a numerical weather prediction model such as WRF to predict local mesoscale conditions. Modeling
415 challenges at this site include non-flat terrain, light precipitation, and unexpected temperature advection. As such, this case study is a major departure from canonical atmospheric and turbine-operating conditions and is expected to build confidence in simulating a wider range of nonstationary atmospheric conditions.

The modeling challenges have been sidestepped by making appropriate assumptions. Assimilating local horizontal wind measurements captured possible terrain-induced flow variability. Even without temperature profile information, assimilating
420 the virtual potential temperature history from a point measurement provided a zero-order representation of temperature and moisture advection. The simulated evolution of wind-engineering quantities (wind speed, wind direction, and turbulence intensity) provided useful inputs to both an engineering wake model and a high-fidelity, LES-based aeroelastic model. The performance of the waked turbine under partially-waked and nearly-waked conditions was satisfactorily reproduced by both models, given the actual measured yaw-offset signal to steer the wake. In addition, the LES was also able to provide high-resolution
425 information about wake dynamics such as wake-induced speedups and wake-steering performance at low wind speeds. This information offers insight into the short-term (intra-hour) variability of wake-steering performance. While performance at these timescales is not of primary concern in the design of a wake-steering control strategy that focuses on optimizing performance over the lifetime of a project, it does suggest that further wake-steering gains are possible and can inform a dynamic set-point selection strategy. A direct outcome of this work is to enable aeroservoelastic simulations of turbines operating in the observed
430 conditions and validate predictions of wake-steering loads. This is detailed in the companion paper by Shaler et al. (2023), which compares the simulated response of turbines T2 and T3 with SCADA signals and available loads measurements.

The tailored MMC approach applied herein distills the relevant flow features from available data and highlights the challenges associated with microscale data assimilation. Flow-field reconstruction challenges will always be site- and case-specific considering, e.g., the difficulty and cost of obtaining temperature profiles at high spatiotemporal resolution. To minimize

435 assumptions needed to create a full wind and temperature profile history for LES, adequate resolution would ideally mean measurements with spacing comparable to the simulated grid spacing (e.g., less than 100 m), up to the top of simulated domain (e.g., 1–2 km), at a sub-hourly sampling frequency. These guidelines should be taken into account when designing field campaigns to complement high-fidelity flow simulations. Even if high-resolution data were available, the microscale LES solution would still be sensitive to the chosen assimilation approach and whether it is desirable to exactly enforce measurements, i.e.,

440 the DPA approach. Currently, no established approach is perfect—DPA can produce excessive turbulence, confirming previous findings (Allaerts et al., 2020); IPA forcings may be unrealistic. In this case, partial DPA provides a viable alternative when the mesoscale flow information is incomplete. Engineering approximations such as IPA or partial DPA are attractive given that every dataset has unique limitations. Moreover, as seen in this study, profile assimilation is not necessarily needed to model an evolving CBL. Therefore, the MMC forcing approach presents an opportunity for further generalization. Future work should

445 focus on development of more robust, mathematically rigorous, and/or physically consistent forcing strategies.

Appendix A: Simulation Codes Used

A1   High-Fidelity Flow Model: SOWFA

We use the Simulator for Wind Farm Applications (SOWFA, Churchfield et al. (2012)), based on OpenFOAM version 6, to

450 perform LESs of the field campaign site. SOWFA solves the momentum and potential temperature transport equations for a dry, incompressible flow with buoyancy effects represented by the Boussinesq approximation. The effects of moisture are accounted for through the use of virtual potential temperature in the temperature transport equation. Individual turbines are represented by actuator disk models (ADM); these turbine aerodynamics models are loosely coupled to OpenFAST (Appendix A2) for a two-way, loosely coupled aeroservoelastic analysis. The term loose coupling is used here to describe a model with two

455 separate dynamics solvers that exchange flow-field velocities (from SOWFA to OpenFAST) and blade aerodynamic forces (from OpenFAST to SOWFA) at periodic intervals.

A2   Aeroservoelastic Model: OpenFAST/ROSCO

OpenFAST (NREL, 2020) is a turbine model that solves the aero-servo-elastic dynamics of individual turbines. Blade aerodynamics are calculated according to blade element theory, from inflow provided by SOWFA. Momentum theory wake modeling

460 is not needed because induction is captured by the SOWFA LES. Blade structural dynamics are calculated according to Euler-Bernoulli beam theory. The turbine controller is provided by the Reference Open-Source Controller (ROSCO, Abbas et al. (2022)), which has been tuned for this particular turbine model. In lieu of a yaw controller, the NREL-measured nacelle yaw

angle of T2 (the controlled turbine) and T3 are specified for the simulated T2 and T3. The yaw positions of turbines T1, T4, and T5 are based on adjusted SCADA signals.

465   In creating the aeroservoelastic model for this study, NREL's reference model behavior, based on measurements of a similar DOE turbine (Santos et al., 2015), was found to differ from the turbines in the field campaign. Moreover, the exact turbine calibrations by the owner–operator are not known, which motivated the tuning of a site-specific turbine aeroservoelastic model. The dynamic response of turbine T2 differed significantly from the other turbines in the test array. This work therefore employed two different ROSCO controllers, with different settings for T2 compared to the other turbines.

470 **A3   Engineering Wake Model: FLORIS**

The Flow Redirection In Steady State (FLORIS) wake model is the same tool that was used to derive the yaw schedule for the field campaign. We apply FLORIS using more recent developments to the wake model that include secondary wake steering and yaw-added wake recovery (King et al., 2021). Because it is not a time-series analysis, we only expect FLORIS to accurately predict trends over the lifetime of a wind project (∼20 years), aggregating the effects of interannual, seasonal,

475   and diurnal variability and neglecting transient weather events. We do not necessarily expect agreement with instantaneous or 10-min-averaged conditions.

Appendix B: Large-Eddy Simulation Setup

All large-eddy simulations were run in a 4 km × 4 km × 1 km domain encompassing the wind farm. A precursor simulation evolves the diurnal ABL before, during, and after the turbine periods of interest; a subsequent turbine simulation restarting from

480   the precursor introduces modeled turbines with mesh refinement around the individual turbines. The ABL turbulence field is resolved on a grid with uniform 10-m spacing and 0.5 s time steps. Initial conditions (previously discussed in Section 4.1) are specified by the nearest upwind sounding.

The precursor domain has periodic lateral boundaries; a no-slip lower boundary with specified time-varying, uniform surface heat flux; and a free-slip upper boundary with fixed temperature gradient dictated by upper-air sounding measurements. On

485   the lower boundary, the surface shear stress is modeled following Schumann (1975), with an assumed aerodynamic roughness length of 0.1 m. Surface heat flux is the measured kinematic heat flux from the met mast at 10 m. SGS turbulence is modeled by the Deardorff turbulence kinetic energy model (Deardorff, 1980). Nonstationary conditions are imposed through momentum and temperature source terms derived from a combination of met mast and lidar data. Mesoscale forcing profiles are updated at the standard wind-engineering time scale—10 minutes—which is shorter than the time scale of mesoscale flow evolution.

490   The turbine simulations restarted from the diurnal precursor simulation at 07:30 UTC on 2019-12-26, 18 minutes prior to the first loads period of interest. Turbines are represented in the LES by the actuator disk model, which has been validated for both wake velocity deficit and power predictions in wind-tunnel experiments (e.g., Neunaber et al. (2021)) and simulations (e.g., Reynolds-Averaged Navier-Stokes simulations Simisiroglou et al. (2017) and LES Lignarolo et al. (2016); Revaz and Porté-Agel (2021)). A single mesh refinement region was added, extending $2.5D$ (D: rotor diameter) upstream and laterally from

495 all turbines, and $15D$ downstream. This refinement region was oriented along the mean hub-height-measured wind direction during the entire turbine simulation, approximately $337°$ (Figure 9). Subsequently, the finest grid spacing was 5-m and the simulation was advanced with 0.25 s time steps.

To model flow through a finite domain in the turbine simulation, the lateral boundary conditions were switched from periodic to a time-varying mixed inlet–outlet condition on the northern, western, and eastern boundaries—the southern boundary was

500 assumed to have only outflow for the duration of the turbine simulation. On the mixed boundaries, each grid face is allowed to operate with inflow or outflow, determined by the sign of the instantaneous velocity flux. This mixed inflow–outflow condition therefore permits significant wind direction variations on a boundary with height and over time. The inflow boundary faces behave as a Dirichlet boundary condition with wind vectors and virtual potential temperatures set from time-varying boundary planes recorded from the precursor, whereas outflow boundary faces behave as a Neumann boundary condition with zero

505 gradient. To maintain mass continuity, the flux on all outflow faces are scaled so that the total outflow exactly matches the total inflow. Dirichlet boundary data are updated at the same time intervals as the mesoscale forcing.

Appendix C: Wind Field Reconstruction

The following steps were taken to reconstruct a full time–height history of wind speeds for MMC given limited field measurements (Figure 5):

510 1. Quality control of measurements: Filter available lidar data by carrier-to-noise ratio (CNR > -22.5 dB for this instrument) and greater than 50% data availability. The threshold was chosen to be relatively low to provide more wind-profile data during the daytime of this particular day. These quality controlled data are shown on the left panel of Figure 5.

2. Power-law wind-profile approximation: Power-law wind-speed profiles $U(z) = U_{ref}(z/z_{ref})^\alpha$ are calculated at 10-min intervals based on i) sonic data alone, which provide high-frequency, high-quality measurements at two heights; ii) all

515 available met-mast measurements, including the sonic anemometers and the cup anemometer (three heights); and iii) all available measurements, which include met-mast sensors and quality controlled lidar data (between 3 and 10 heights, depending on lidar CNR). The shear exponent (α) is estimated from 10-min mean wind-speed measurements and the reference height in all three cases is taken to be the 50-m sonic anemometer measurement.

3. Quality control of approximate wind profiles: The instantaneous power-law profiles are filtered by the Pearson correlation

520 coefficient (R^2). While the sonic-only profiles have a perfect $R^2 = 1$ for any $U(z)$ that increases with height, $R^2 < 1$ in general. At every instant, the power-law fit with R^2 above a threshold of 0.9 with the most number of data heights is selected. The conclusion of this step provides continuous wind profiles that increase monotonically with height up to the highest measurement height.

4. Vertical spline interpolation: When R^2 is less than the threshold, but lidar data are available up to the maximum range

525 (180 m during the case day), these non-power-law-conforming or transient profiles are represented by piecewise cubic Hermite polynomials with $U(z = 0) = 0$. Near the surface, however, spline interpolation tended to underpredict the wind

shear and overpredict wind speeds by approximately 1 m/s at the center of the first computational cell (5-m AGL). As a workaround, the wind profile from the power-law fit with two sonic anemometer measurements, up to 50 m, was combined with the spline-interpolated profile between 50 m and 180 m—spline extrapolation was not performed.

530   5. Linear interpolation: Linear interpolation was used to infill the profiles over time where neither a profile-law fit nor spline interpolation was performed. Above the highest measurement height height, the wind is assumed to be constant. The final result is shown on the right panel of Figure 5.

The time–height history of wind directions was generated in a more simplistic manner. Without an approximate profile (analogous to the power law for wind speeds), spline interpolation was applied between the lowest and highest available
535 measurement. Wind directions at the surface and above the highest measurement were back- and forward-filled, respectively.

Author contributions. EQ performed the data analysis; defined the case study; developed the coupled simulation strategy; setup, executed, and postprocessed all simulations; interpreted the results; and prepared the manuscript.

Competing interests. EQ has no competing interests.

Disclaimer. The views expressed in the article do not necessarily represent the views of the DOE or the U.S. Government. The U.S. Gov-
540 ernment retains and the publisher, by accepting the article for publication, acknowledges that the U.S. Government retains a nonexclusive, paid-up, irrevocable, worldwide license to publish or reproduce the published form of this work, or allow others to do so, for U.S. Government purposes.

Acknowledgements. The author thanks the NREL instrumentation team that collected these experimental data as well as Matthew Church-
field, Paula Doubrawa, and Jason Jonkman for supporting this effort through their respective projects.
545   This work was authored by the National Renewable Energy Laboratory, operated by Alliance for Sustainable Energy, LLC, for the U.S. Department of Energy (DOE) under contract no. DE-AC36-08GO28308. Funding was provided by the U.S. Department of Energy Office of Energy Efficiency and Renewable Energy Wind Energy Technologies Office.

References

Abbas, N. J., Zalkind, D. S., Pao, L., and Wright, A.: A Reference Open-Source Controller for Fixed and Floating Offshore Wind Turbines,
550 Wind Energy Science, 7, 53–73, https://doi.org/10.5194/wes-7-53-2022, 2022.

Abkar, M., Sharifi, A., and Porté-Agel, F.: Wake Flow in a Wind Farm during a Diurnal Cycle, Journal of Turbulence, 17, 420–441,
https://doi.org/10.1080/14685248.2015.1127379, 2016.

Allaerts, D., Quon, E., and Churchfield, M.: Using Observational Mean-flow Data to Drive Large-eddy Simulations of a Diurnal Cycle at the
SWiFT Site, Wind Energy, p. we.2811, https://doi.org/10.1002/we.2811, 2023.

555 Allaerts, D. J. N., Quon, E., Draxl, C., and Churchfield, M.: Development of a Time–Height Profile Assimilation Technique for Large-Eddy
Simulation, Boundary-Layer Meteorology, 176, https://doi.org/10.1007/s10546-020-00538-5, 2020.

Angevine, W. M., Edwards, J. M., Lothon, M., LeMone, M. A., and Osborne, S. R.: Transition Periods in the Diurnally-Varying Atmospheric
Boundary Layer Over Land, Boundary-Layer Meteorology, 177, 205–223, https://doi.org/10.1007/s10546-020-00515-y, 2020.

Arthur, R. S., Mirocha, J. D., Marjanovic, N., Hirth, B. D., Schroeder, J. L., Wharton, S., and Chow, F. K.: Multi-Scale Simulation of Wind
560 Farm Performance during a Frontal Passage, Atmosphere, 11, 245, https://doi.org/10.3390/atmos11030245, 2020.

Basu, S., Holtslag, A. A. M., Wiel, B. J. H. V. D., Moene, A. F., and Steeneveld, G.-J.: An Inconvenient "Truth" about Using
Sensible Heat Flux as a Surface Boundary Condition in Models under Stably Stratified Regimes, Acta Geophysica, 56, 88–99,
https://doi.org/10.2478/s11600-007-0038-y, 2008a.

Basu, S., Vinuesa, J.-F., and Swift, A.: Dynamic LES Modeling of a Diurnal Cycle, Journal of Applied Meteorology and Climatology, 47,
565 1156–1174, https://doi.org/10.1175/2007JAMC1677.1, 2008b.

Berg, L. K., Liu, Y., Yang, B., Qian, Y., Olson, J., Pekour, M., Ma, P.-L., and Hou, Z.: Sensitivity of Turbine-Height Wind Speeds to Param-
eters in the Planetary Boundary-Layer Parametrization Used in the Weather Research and Forecasting Model: Extension to Wintertime
Conditions, Boundary-Layer Meteorology, 170, 507–518, https://doi.org/10.1007/s10546-018-0406-y, 2019.

Bosveld, F. C., Baas, P., Steeneveld, G.-J., Holtslag, A. A. M., Angevine, W. M., Bazile, E., de Bruijn, E. I. F., Deacu, D., Edwards,
570 J. M., Ek, M., Larson, V. E., Pleim, J. E., Raschendorfer, M., and Svensson, G.: The Third GABLS Intercomparison Case for Eval-
uation Studies of Boundary-Layer Models. Part B: Results and Process Understanding, Boundary-Layer Meteorology, 152, 157–187,
https://doi.org/10.1007/s10546-014-9919-1, 2014a.

Bosveld, F. C., Baas, P., van Meijgaard, E., de Bruijn, E. I. F., Steeneveld, G.-J., and Holtslag, A. A. M.: The Third GABLS Intercomparison
Case for Evaluation Studies of Boundary-Layer Models. Part A: Case Selection and Set-Up, Boundary-Layer Meteorology, 152, 133–156,
575 https://doi.org/10.1007/s10546-014-9917-3, 2014b.

Branlard, E. and Meyer Forsting, A. R.: Assessing the Blockage Effect of Wind Turbines and Wind Farms Using an Analytical Vortex Model,
Wind Energy, 23, 2068–2086, https://doi.org/10.1002/we.2546, 2020.

Churchfield, M. J., Lee, S., Michalakes, J., and Moriarty, P. J.: A Numerical Study of the Effects of Atmospheric and Wake Turbulence on
Wind Turbine Dynamics, Journal of Turbulence, 13, 1–32, https://doi.org/10.1080/14685248.2012.668191, 2012.

580 Deardorff, J. W.: Stratocumulus-Capped Mixed Layers Derived from a Three-Dimensional Model, Boundary-Layer Meteorology, 18, 495–
527, 1980.

Doekemeijer, B. M., Simley, E., and Fleming, P.: Comparison of the Gaussian Wind Farm Model with Historical Data of Three Offshore
Wind Farms, Energies, 15, 1964, https://doi.org/10.3390/en15061964, 2022.

Draxl, C., Allaerts, D., Quon, E., and Churchfield, M.: Coupling Mesoscale Budget Components to Large-Eddy Simulations for Wind-Energy Applications, Boundary-Layer Meteorology, 179, 73–98, https://doi.org/10.1007/s10546-020-00584-z, 2021.

Duynkerke, P. G., de Roode, S. R., van Zanten, M. C., Calvo, J., Cuxart, J., Cheinet, S., Chlond, A., Grenier, H., Jonker, P. J., Köhler, M., Lenderink, G., Lewellen, D., Lappen, C.-L., Lock, A. P., Moeng, C.-H., Müller, F., Olmeda, D., Piriou, J.-M., Sánchez, E., and Sednev, I.: Observations and Numerical Simulations of the Diurnal Cycle of the EUROCS Stratocumulus Case, Quarterly Journal of the Royal Meteorological Society, 130, 3269–3296, https://doi.org/10.1256/qj.03.139, 2004.

Fleming, P., King, J., Dykes, K., Simley, E., Roadman, J., Scholbrock, A., Murphy, P., Lundquist, J. K., Moriarty, P., Fleming, K., van Dam, J., Bay, C., Mudafort, R., Lopez, H., Skopek, J., Scott, M., Ryan, B., Guernsey, C., and Brake, D.: Initial Results from a Field Campaign of Wake Steering Applied at a Commercial Wind Farm – Part 1, Wind Energy Science, 4, 273–285, https://doi.org/doi.org/10.5194/wes-4-273-2019, 2019.

Fleming, P., King, J., Simley, E., Roadman, J., Scholbrock, A., Murphy, P., Lundquist, J. K., Moriarty, P., Fleming, K., van Dam, J., Bay, C., Mudafort, R., Jager, D., Skopek, J., Scott, M., Ryan, B., Guernsey, C., and Brake, D.: Continued Results from a Field Campaign of Wake Steering Applied at a Commercial Wind Farm – Part 2, Wind Energy Science, 5, 945–958, https://doi.org/10.5194/wes-5-945-2020, 2020.

Hannesdóttir, Á., Kelly, M., and Dimitrov, N.: Extreme Wind Fluctuations: Joint Statistics, Extreme Turbulence, and Impact on Wind Turbine Loads, Wind Energy Science, 4, 325–342, https://doi.org/10.5194/wes-4-325-2019, 2019.

Haupt, S., Berg, L., Decastro, A., Gagne, D., Jimenez, P., Juliano, T., Kosovic, B., Quon, E., Shaw, W., Churchfield, M., Draxl, C., Hawbecker, P., Jonko, A., Kaul, C., Mirocha, J., and Rai, R.: Outcomes of the DOE Workshop on Atmospheric Challenges for the Wind Energy Industry, Tech. Rep. PNNL–30828, 1762812, https://doi.org/10.2172/1762812, 2020.

Haupt, S. E., Kosovic, B., Shaw, W., Berg, L. K., Churchfield, M., Cline, J., Draxl, C., Ennis, B., Koo, E., Kotamarthi, R., Mazzaro, L., Mirocha, J., Moriarty, P., Muñoz-Esparza, D., Quon, E., Rai, R. K., Robinson, M., and Sever, G.: On Bridging a Modeling Scale Gap: Mesoscale to Microscale Coupling for Wind Energy, Bulletin of the American Meteorological Society, 100, https://doi.org/10.1175/BAMS-D-18-0033.1, 2019.

Howland, M. F., Ghate, A. S., Quesada, J. B., Pena Martínez, J. J., Zhong, W., Larrañaga, F. P., Lele, S. K., and Dabiri, J. O.: Optimal Closed-Loop Wake Steering – Part 2: Diurnal Cycle Atmospheric Boundary Layer Conditions, Wind Energy Science, 7, 345–365, https://doi.org/10.5194/wes-7-345-2022, 2022.

Jayaraman, B., Quon, E., Li, J., and Chatterjee, T.: Structure of Offshore Low-Level Jet Turbulence and Implications to Mesoscale-to-Microscale Coupling, Journal of Physics: Conference Series, 2265, 022 064, https://doi.org/10.1088/1742-6596/2265/2/022064, 2022.

Jiménez, P. A. and Dudhia, J.: On the Ability of the WRF Model to Reproduce the Surface Wind Direction over Complex Terrain, Journal of Applied Meteorology and Climatology, 52, 1610–1617, https://doi.org/10.1175/JAMC-D-12-0266.1, 2013.

King, J., Fleming, P., King, R., Martínez-Tossas, L. A., Bay, C. J., Mudafort, R., and Simley, E.: Control-Oriented Model for Secondary Effects of Wake Steering, Wind Energy Science, 6, 701–714, https://doi.org/10.5194/wes-6-701-2021, 2021.

Kleczek, M. A., Steeneveld, G.-J., and Holtslag, A. A. M.: Evaluation of the Weather Research and Forecasting Mesoscale Model for GABLS3: Impact of Boundary-Layer Schemes, Boundary Conditions and Spin-Up, Boundary-Layer Meteorology, 152, 213–243, https://doi.org/10.1007/s10546-014-9925-3, 2014.

Kumar, V., Kleissl, J., Meneveau, C., and Parlange, M. B.: Large-Eddy Simulation of a Diurnal Cycle of the Atmospheric Boundary Layer: Atmospheric Stability and Scaling Issues: LES OF A DIURNAL CYCLE OF THE ABL, Water Resources Research, 42, https://doi.org/10.1029/2005WR004651, 2006.

Kumar, V., Svensson, G., Holtslag, A. A. M., Meneveau, C., and Parlange, M. B.: Impact of Surface Flux Formulations and Geostrophic Forcing on Large-Eddy Simulations of Diurnal Atmospheric Boundary Layer Flow, Journal of Applied Meteorology and Climatology, 49, 1496–1516, https://doi.org/10.1175/2010JAMC2145.1, 2010.

Lignarolo, L. E., Mehta, D., Stevens, R. J., Yilmaz, A. E., van Kuik, G., Andersen, S. J., Meneveau, C., Ferreira, C. J., Ragni, D., Meyers, J., van Bussel, G. J., and Holierhoek, J.: Validation of Four LES and a Vortex Model against Stereo-PIV Measurements in the near Wake of an Actuator Disc and a Wind Turbine, Renewable Energy, 94, 510–523, https://doi.org/10.1016/j.renene.2016.03.070, 2016.

Liu, Y., Bourgeois, A., Warner, T., and Swerdlin, S.: An "Observation-Nudging"-Based FDDA Scheme for WRF-ARW for Mesoscale Data Assimilation and Forecasting, in: 4th Symposium on Space Weather, p. 6, San Antonio, Texas, 2007.

Meyers, J., Bottasso, C., Dykes, K., Fleming, P., Gebraad, P., Giebel, G., Göçmen, T., and van Wingerden, J.-W.: Wind Farm Flow Control: Prospects and Challenges, Wind Energy Science, 7, 2271–2306, https://doi.org/10.5194/wes-7-2271-2022, 2022.

Mirocha, J. D., Rajewski, D. A., Marjanovic, N., Lundquist, J. K., Kosović, B., Draxl, C., and Churchfield, M. J.: Investigating Wind Turbine Impacts on Near-Wake Flow Using Profiling Lidar Data and Large-Eddy Simulations with an Actuator Disk Model, Journal of Renewable and Sustainable Energy, 7, 043 143, https://doi.org/10.1063/1.4928873, 2015.

Neunaber, I., Hölling, M., Whale, J., and Peinke, J.: Comparison of the Turbulence in the Wakes of an Actuator Disc and a Model Wind Turbine by Higher Order Statistics: A Wind Tunnel Study, Renewable Energy, 179, 1650–1662, https://doi.org/10.1016/j.renene.2021.08.002, 2021.

NREL: OpenFAST. Version 2.4.0, https://github.com/OpenFAST/openfast, 2020.

Porté-Agel, F.: Wind-Turbine and Wind-Farm Flows: A Review, Boundary-Layer Meteorology, 174, 1–59, https://doi.org/doi://10.1007/s10546-019-00473-0, 2020.

Revaz, T. and Porté-Agel, F.: Large-Eddy Simulation of Wind Turbine Flows: A New Evaluation of Actuator Disk Models, Energies, 14, 3745, https://doi.org/10.3390/en14133745, 2021.

Rodrigo, J. S., Allaerts, D., Avila, M., Barcons, J., Cavar, D., Arroyo, R. C., Churchfield, M., Kosovic, B., JK Lundquist, Meyers, J., Esparza, D. M., Palma, J., Tomaszewski, J. M., Troldborg, N., van der Laan, M., and Rodrigues, C. V.: Results of the GABLS3 Diurnal-Cycle Benchmark for Wind Energy Applications, Journal of Physics: Conference Series, 854, 012 037, https://doi.org/10.1088/1742-6596/854/1/012037, 2017.

Santoni, C., García-Cartagena, E. J., Ciri, U., Zhan, L., Valerio Iungo, G., and Leonardi, S.: One-Way Mesoscale-Microscale Coupling for Simulating a Wind Farm in North Texas: Assessment against SCADA and LiDAR Data, Wind Energy, 23, 691–710, https://doi.org/10.1002/we.2452, 2020.

Santos, R., van Dam, J., and Santos Wind Engineering Technologies, Inc., Portland, Maine: Mechanical Loads Test Report for the U.S. Department of Energy 1.5-Megawatt Wind Turbine, Tech. Rep. NREL/TP–5000-63679, 1215119, https://doi.org/10.2172/1215119, 2015.

Sanz Rodrigo, J., Chávez Arroyo, R. A., Moriarty, P., Churchfield, M., Kosović, B., Réthoré, P.-E., Hansen, K. S., Hahmann, A., Mirocha, J. D., and Rife, D.: Mesoscale to Microscale Wind Farm Flow Modeling and Evaluation, WIREs Energy and Environment, 6, https://doi.org/10.1002/wene.214, 2017.

Sanz Rodrigo, J., Santos, P., Chávez Arroyo, R., Avila, M., Cavar, D., Lehmkuhl, O., Owen, H., Li, R., and Tromeur, E.: The ALEX17 Diurnal Cycles in Complex Terrain Benchmark, Journal of Physics: Conference Series, 1934, 012 002, https://doi.org/10.1088/1742-6596/1934/1/012002, 2021.

Schalkwijk, J., Jonker, H. J. J., Siebesma, A. P., and Bosveld, F. C.: A Year-Long Large-Eddy Simulation of the Weather over Cabauw: An Overview, Monthly Weather Review, 143, 828–844, https://doi.org/10.1175/MWR-D-14-00293.1, 2015.

Schumann, U.: Subgrid Scale Model for Finite Difference Simulations of Turbulent Flows in Plane Channels and Annuli, Journal of Com-
660   putational Physics, 18, 376–404, https://doi.org/10.1016/0021-9991(75)90093-5, 1975.

Shaler, K., Quon, E., and Jonkman, J.: Wind Farm Structural Response and Wake Evolution Undergoing Wake Steering for an Evolving
Stable Boundary Layer: Computational and Experimental Comparisons, Submitted to Wind Energy Science, 2023.

Simisiroglou, N., Breton, S.-P., and Ivanell, S.: Validation of the Actuator Disc Approach Using Small-Scale Model Wind Turbines, Wind
Energy Science, 2, 587–601, https://doi.org/10.5194/wes-2-587-2017, 2017.

665   Stauffer, D. R. and Seaman, N. L.: Multiscale Four-Dimensional Data Assimilation, Journal of Applied Meteorology, 33, 416–434,
https://doi.org/10.1175/1520-0450(1994)033<0416:MFDDA>2.0.CO;2, 1994.

Stoll, R., Gibbs, J. A., Salesky, S. T., Anderson, W., and Calaf, M.: Large-Eddy Simulation of the Atmospheric Boundary Layer, Boundary-
Layer Meteorology, 177, 541–581, https://doi.org/10.1007/s10546-020-00556-3, 2020.

Sun, J., Lenschow, D. H., Burns, S. P., Banta, R. M., Newsom, R. K., Coulter, R., Frasier, S., Ince, T., Nappo, C., Balsley, B. B., Jensen, M.,
670   Mahrt, L., Miller, D., and Skelly, B.: Atmospheric Disturbances That Generate Intermittent Turbulence in Nocturnal Boundary Layers,
Boundary-Layer Meteorology, 110, 255–279, https://doi.org/10.1023/A:1026097926169, 2004.

Telford, P. J., Braesicke, P., Morgenstern, O., and Pyle, J. A.: Technical Note: Description and Assessment of a Nudged Version of the New
Dynamics Unified Model, Atmospheric Chemistry and Physics, 8, 1701–1712, https://doi.org/10.5194/acp-8-1701-2008, 2008.

Vollmer, L., Lee, J. C.-Y., Steinfeld, G., and Lundquist, J. K.: A Wind Turbine Wake in Changing Atmospheric Conditions: LES and Lidar
675   Measurements, Journal of Physics: Conference Series, 854, 012 050, https://doi.org/10.1088/1742-6596/854/1/012050, 2017a.

Vollmer, L., Steinfeld, G., and Kühn, M.: Transient LES of an Offshore Wind Turbine, Wind Energy Science, 2, 603–614,
https://doi.org/10.5194/wes-2-603-2017, 2017b.

Xu, H. H. A. and Yang, X. I. A.: Treatment of Unphysical Numerical Oscillations via Local Grid Refinement, Physics of Fluids, 33, 077 104,
https://doi.org/10.1063/5.0054642, 2021.

680   Yang, B., Qian, Y., Berg, L. K., Ma, P.-L., Wharton, S., Bulaevskaya, V., Yan, H., Hou, Z., and Shaw, W. J.: Sensitivity of Turbine-Height
Wind Speeds to Parameters in Planetary Boundary-Layer and Surface-Layer Schemes in the Weather Research and Forecasting Model,
Boundary-Layer Meteorology, 162, 117–142, https://doi.org/10.1007/s10546-016-0185-2, 2017.

Zajaczkowski, F. J., Haupt, S. E., and Schmehl, K. J.: A Preliminary Study of Assimilating Numerical Weather Prediction Data into
Computational Fluid Dynamics Models for Wind Prediction, Journal of Wind Engineering and Industrial Aerodynamics, 99, 320–329,
685   https://doi.org/10.1016/j.jweia.2011.01.023, 2011.